

# A magnetic resonance study of temperature-dependent microstructural evolution and self-diffusion of water in Arctic first-year sea ice

C. BOCK,<sup>1</sup> H. EICKEN<sup>2</sup>

<sup>1</sup>Alfred Wegener Institute for Polar and Marine Research, PO Box 120161, D-27515 Bremerhaven, Germany

<sup>2</sup>Geophysical Institute, University of Alaska, 903 Koyukuk Drive, Fairbanks, AK 99775-7320, USA

E-mail: [hajo.eicken@gi.alaska.edu](mailto:hajo.eicken@gi.alaska.edu)

**ABSTRACT.** The microstructural evolution of brine inclusions in granular and columnar sea ice has been investigated through magnetic resonance imaging (MRI) for temperatures between  $-28$  and  $-3^{\circ}\text{C}$ . Thin-section and salinity measurements were completed on core samples obtained from winter sea ice near Barrow, Alaska, USA. Subsamples of granular (2–5 cm depth in core) and columnar sea ice (20–23 cm depth) were investigated with morphological spin-echo and diffusion-weighted imaging in a Bruker 4.7T MRI system operating at field gradients of  $200\text{ mT m}^{-1}$  at temperatures of approximately  $-28$ ,  $-15$ ,  $-6$  and  $-3^{\circ}\text{C}$ . Average linear pore dimensions range from 0.2 to 1 mm and increase with bulk liquid volume fraction as temperatures rise from  $-15$  to  $-3^{\circ}\text{C}$ . Granular ice pores are significantly larger than columnar ice pores and exhibit a higher degree of connectivity. No evidence is found of strongly non-linear increases in pore connectivity based on the MRI data. This might be explained by shortcomings in resolution, sensitivity and lack of truly three-dimensional data, differences between laboratory and field conditions or the absence of a percolation transition. Pore connectivity increases between  $-6$  and  $-3^{\circ}\text{C}$ . Pore-number densities average at  $1.4 \pm 1.2\text{ mm}^{-2}$ . The pore-number density distribution as a function of cross-sectional area conforms with power-law and lognormal distributions previously identified, although significant variations occur as a function of ice type and temperature. At low temperatures ( $< -26^{\circ}\text{C}$ ), pore sizes were estimated from  $^1\text{H}$  self-diffusivity measurements, with self-diffusivity lower by up to an order of magnitude than in the free liquid. Analysis of diffusional length scales suggests characteristic pore dimensions of  $< 1\text{ }\mu\text{m}$  at  $< -26^{\circ}\text{C}$ .

## 1. INTRODUCTION

The pore microstructure and permeability of sea ice are of significant relevance for ocean–atmosphere heat transfer (Hudier and others, 1995; Lytle and Ackley, 1996; Eicken and others, 2002), the exchange of dissolved and particulate matter (Freitag, 1999; Krembs and others, 2000) as well as the salinity evolution of the ice cover (Wettlaufer and others, 2000). Ice permeability depends strongly on the microstructure, in particular connectivity, of pores, which has not been examined in much detail to date. In fact, the pioneering study by Assur (1960) with a model of pore morphology evolving as a function of temperature still defines the state of the art. While Perovich and Gow (1996) have since provided quantitative information on pore-size distributions, this has not led to a closer examination of brine-pocket connectivity. Golden and others (1998) postulated that highly non-linear transitions in sea-ice permeability and other transport properties as a function of brine-volume fraction (assumed to be chiefly driven by temperature) can be explained by percolation theory, expressing the permeability as a function of brine-volume fraction relative to a critical porosity threshold and a critical exponent. It is assumed that at the percolation threshold the linking of pores and the establishment of larger-scale conduit networks is responsible for the increase in permeability and other transport properties. Wettlaufer and others (2000) found that brine transport transitions depend on a critical Rayleigh number, which in turn is dependent upon ice thickness, temperature and permeability.

Observations of microstructural changes that could drive transitions in permeability are difficult to obtain, as standard pore analysis techniques are destructive and often involve substantial changes in ice temperature (Perovich and Gow, 1996). Light and others (2003) studied thermally driven microstructural changes on ice thick sections at spatial scales mostly relevant for ice optical properties and radiative transfer. Other potentially promising means of obtaining data on microstructural transformations are non-destructive methods such as X-ray computed tomography (Kawamura, 1988) or magnetic resonance (MR) techniques. MR images for NaCl ice were first obtained by Edelstein and Schulson (1991) with a low-resolution system. Callaghan and others (1999) have advanced the use of in situ MR techniques to obtain estimates of bulk ice porosity and diffusive and advective brine transport. Menzel and others (2000) and Menzel (2002) employed a combination of MR imaging (MRI) techniques to obtain data on brine diffusivity in artificially grown sea ice. Eicken and others (2000) examined changes in pore microstructure between  $-21$  and  $-6^{\circ}\text{C}$  at higher MRI resolution.

Here, we employ MRI and bulk diffusivity measurements to examine pore evolution over a temperature range of  $-28$  to  $-3^{\circ}\text{C}$  for granular and columnar first-year sea ice obtained near Barrow, Alaska, USA, assessing changes in pore morphology and connectivity relevant for transport processes. Furthermore, measurements of self-diffusive length scales with MR techniques have been employed to probe pore dimensions at low temperatures where the spatial resolution of MRI is insufficient.

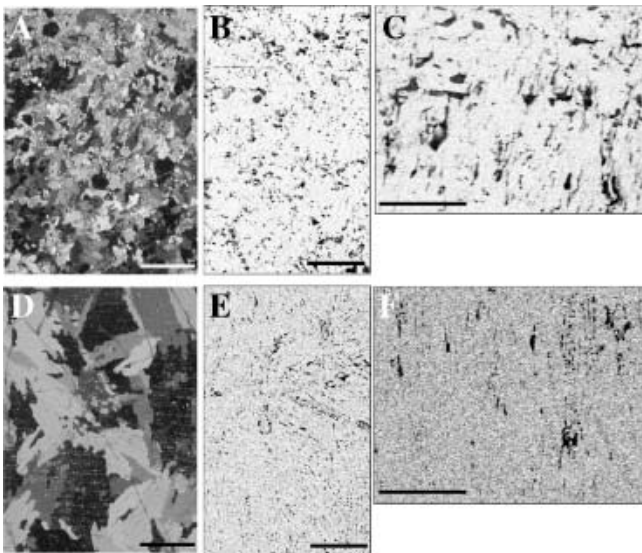


**Fig. 1.** Grain and pore microstructure of granular ice (2–5 cm depth) (A–C) and columnar ice (20–23 cm depth) (D–F) sampled near Barrow. Shown are horizontal thin sections between crossed polarizers (A, D) and horizontal (B, E) and vertical (C, F) MRI slices with pores appearing dark. Scale bar is 10 mm long. MRI data were obtained at roughly  $-3^{\circ}\text{C}$ .

## 2. METHODS AND MATERIALS

Core samples of young sea ice were obtained from Elson Lagoon, near Barrow, in November 2000, employing standard methods as described in Eicken and others (2000). Undeformed sea ice in the Barrow region is quite homogeneous and has been shown to be representative of Arctic first-year sea ice (Weeks, 2001). At the time of

sampling, ice thickness was 28–32 cm with 3 cm of snow. Ice temperatures ranged from  $-9^{\circ}\text{C}$  in the ice surface layer to  $-4^{\circ}\text{C}$  in the ice interior to  $-2^{\circ}\text{C}$  at the bottom. After sampling, cores were cooled to  $-25^{\circ}\text{C}$  and transferred to the Geophysical Institute, University of Alaska Fairbanks, USA, and the Alfred Wegener Institute, Bremerhaven, Germany, while maintaining temperatures to within  $\pm 2\text{ K}$ .

In Fairbanks, ice thick and thin sections were produced and salinity was measured on melted core sections with a YSI model 30 conductivity probe. Based on core stratigraphy, two subsamples were cut from a parallel core sample at 2–5 cm and 20–23 cm depth and prepared for MRI in the Bremerhaven laboratory (for details of analysis technique, see Eicken and others, 2000). Ice blocks  $6 \times 4 \times 3\text{ cm}^3$  in size were placed in a sample chamber, equipped with a fiber-optic probe for determination of in situ ice temperatures inside the MR. In order to maintain constant temperatures, the sample containers were kept in a cooling unit (stable to  $\pm 1\text{ K}$  from setpoint). Experiments were carried out in a Bruker Biospec 4.7T scanner equipped with a mini-imaging unit (maximum gradient strengths of  $200\text{ mT m}^{-1}$ ). Cylindrical probes adapted to high-conductivity samples were used for signal transmission and detection (9 cm diameter). For morphological studies a multi-slice, multi-echo (MSME) sequence was used (matrix size  $512 \times 256$ , axial field of view (FOV)  $3.6 \times 3\text{ cm}^2$ , slice thickness 0.4 mm, 6–12 slices, slice separation 4.6 mm, RF pulses: sinc3 of  $3000\mu\text{s}$ , time to repetition (TR)=540 ms, time to echo (TE)=40 ms, 24 averages, acquisition time 2 hours). Diffusion-weighted imaging (DWI) was conducted using a 3- to 4-point Stejskal–Tanner pulsed gradient spin-echo sequence (parameters:  $128 \times 128$ , FOV  $3.6 \times 3\text{ cm}^2$ , 9 slices, slice thickness 0.4 mm, slice separation 4.6 mm, sinc3 of  $3000\mu\text{s}$ , 8 averages, acquisition time 20 min,

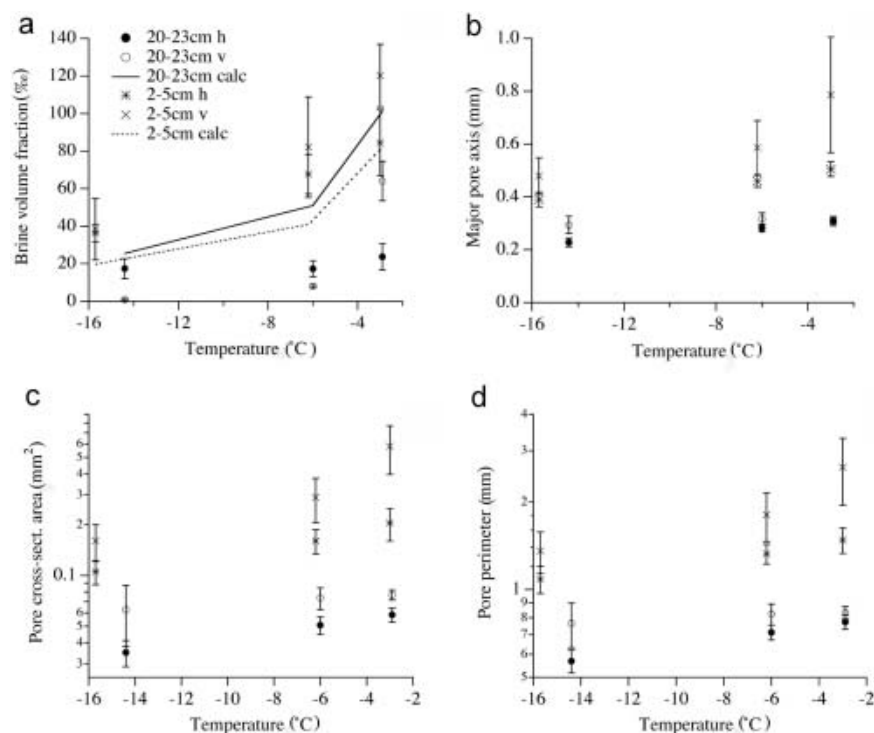


**Fig. 2.** Pore microstructural variables obtained for horizontal (h) and vertical (v) MRI slices as a function of temperature. For these and all subsequent figures, consistent symbols are used to distinguish between different samples and orientations. Lines shown in (a) correspond to brine-volume fractions calculated from phase relations for bulk salinity and temperature of each sample.

big delta = 18.93 ms,  $b$  values: 11, 316, 623, 930 s mm<sup>-2</sup>). MSME and DWI were completed at four constant temperatures attained while warming the samples from approximately  $-28$  to  $-3^{\circ}\text{C}$ . All measurements were completed on natural samples, i.e. without centrifugation or injection of contrast agent such as decane (cf. Eicken and others, 2000).

### 3. RESULTS

#### 3.1. Magnetic-resonance imaging of pores

Based on stratigraphic analysis, subsamples of granular ice (2–5 cm depth; Fig. 1a–c), originating from frazil ice growth during the early stages of ice formation, approximately 1 month prior to sampling, and columnar ice (20–23 cm depth; Fig. 1d–f), formed through congelation growth at the base of the ice sheet, were studied with MRI techniques. Horizontal and vertical MRI slices near the center of the sample obtained at  $-3^{\circ}\text{C}$  are shown in Figure 1. As the method is sensitive to the volume fraction of  $^1\text{H}$  present in the liquid phase, liquid inclusions (dark) can be distinguished from the solid ice matrix (white). The columnar ice exhibits the typical lamellar substructure with vertically oriented layers and tubes of brine inclusions within larger ice grains. Brine inclusions in granular ice are less ordered and of lamellar, tubular or isometric shape. The sea-ice salinity profile exhibits the C shape typical of young ice, with values around 8‰ at top and bottom and 4–6‰ in the ice interior. From the ice salinity and temperature, the in situ brine-volume fractions have been derived according to Cox and Weeks (1983). While salinities are quite similar for both samples (granular ice 5.1‰, columnar ice 5.9‰), brine-volume fractions vary due to higher temperatures in the lower layers of the ice (granular ice 34%, columnar ice 101%).

Based on the liquid volume fraction derived from each MRI volume element, the image data were segmented into ice and pores employing the approach outlined by Eicken and others (2000) and key microstructural variables obtained for horizontal and vertical slices (Fig. 2). Theoretical liquid volume fraction (based on temperature and bulk salinity of the entire sample) and MRI-derived values deviate significantly, with MRI underestimating columnar ice liquid porosity and overestimating granular ice porosity (Fig. 2a). These deviations are in part explained by small-scale variability as apparent in the pore spatial distribution (Fig. 1c and f), particularly in the columnar ice. However, instrumental errors contribute significantly as well. At a  $^1\text{H}$  resonance frequency of 200 MHz, the data are affected by signal loss in the brine (see more detailed discussion in Eicken and others, 2000). In combination with insufficient spatial resolution (at best 0.06 mm in-plane at 0.4 mm slice thickness), this also results in insufficient signal strength at temperatures below about  $-15^{\circ}\text{C}$  (brine-volume fraction <20‰), requiring a different approach for estimates of pore size and morphology, outlined in section 3.2 below. These deviations need to be considered in interpreting other pore microstructural parameters that are tied to total porosity.

Pore dimensions are mostly comparable to those obtained in an earlier study (Eicken and others, 2000). Pores in granular ice are significantly larger than those in columnar ice, with mean cross-sectional areas of 0.1–0.6 and

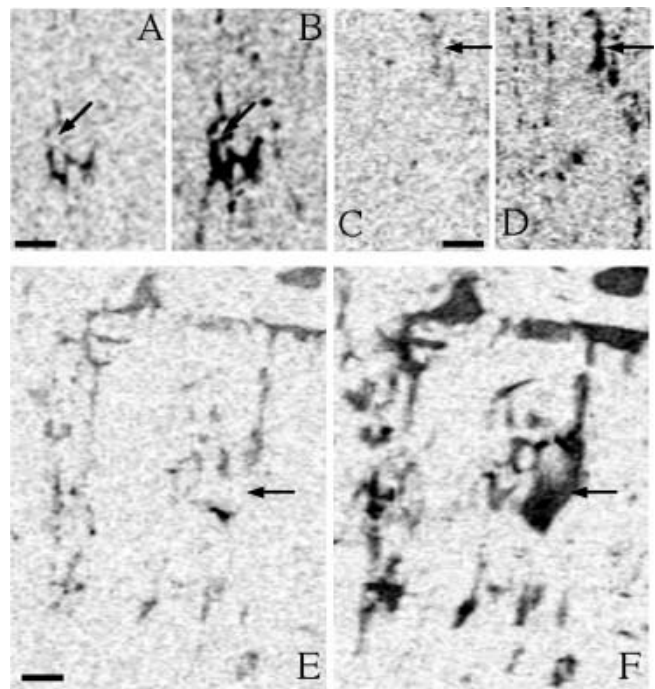


**Fig. 3.** Vertical MRI slices showing pores (dark) in columnar (A–D) and granular (E, F) ice obtained at two different temperatures: (A, C)  $-6.0^{\circ}\text{C}$ ; (B, D)  $-2.9^{\circ}\text{C}$ ; (E)  $-6.2^{\circ}\text{C}$ ; (F)  $-3.0^{\circ}\text{C}$ . Scale bar is 2 mm long. Arrows highlight increased linkage of pores disjoint at lower temperatures.

0.03–0.08 mm<sup>2</sup>, respectively. Apart from the high variability between individual MRI slices, pore linear dimensions (major axis of inscribed ellipse), cross-sectional area and perimeter covary substantially, with the square of either major axis or perimeter explaining 96% and 98% of the variance in pore cross-sectional area for all data points (Fig. 2). Increases in pore dimensions with increasing temperature are explained by porosity increases, with brine-volume fraction explaining 30–40% of the total variance in pore microstructural variables.

As such, the microstructural data (including pore number densities which average at  $1.4 \pm 1.2 \text{ mm}^{-3}$  for all samples and temperatures) provide little if any indication of increases in pore size or connectivity other than those driven by the increase in bulk porosity as the ice is warmed from  $-6$  to  $-3^{\circ}\text{C}$ , corresponding to theoretical bulk liquid volume fractions of 40–100‰ (Fig. 2a). In part, this is due to the fact that most pores are comparatively small, isolated features. Larger brine inclusions appear to merge into more connected features at higher temperatures, however. In columnar ice, this coalescence not only includes the previously described merging of individual brine pockets into tubular inclusions as seen along the direction of the brine and ice lamellae (Fig. 3c and d; see features highlighted by arrows) but also extends to the formation of more complex pore shapes observed within the lamellar plane (Fig. 3a and b). The latter type of pore morphology and increase in connectivity is particularly pronounced in the granular ice (Fig. 3e and f).

#### 3.2 Bulk measurements of self-diffusion of water

Given the limitations of MRI in imaging the smallest pores present in ice, in particular at temperatures well below

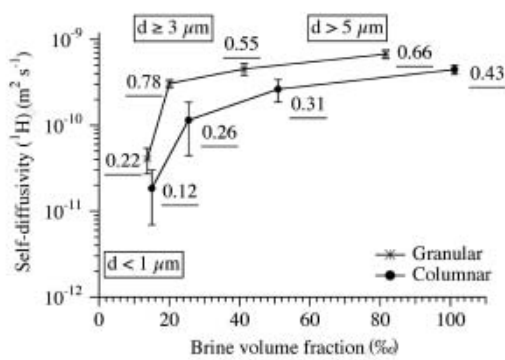


**Fig. 4.** Self-diffusivity, determined for an observation time  $\Delta = 19$  ms, plotted as a function of bulk brine-volume fraction for each sample. The numbers in boxes indicate the magnitude of the characteristic pore size  $d$  over the corresponding porosity interval, as derived from deviations between apparent diffusivity and self-diffusivity of water in the free liquid. Also shown is the relative magnitude of the self-diffusivity, i.e. the ratio between the self-diffusivity measured within brine inclusions divided by that of the free liquid at the same temperature (numbers underlined).

$-15^{\circ}\text{C}$ , we have determined the magnitude of the water (or rather  $^1\text{H}$ ) self-diffusivity integrated over the entire ice volume in the temperature range  $-28$  to  $-3^{\circ}\text{C}$ . The apparent self-diffusivity  $D$  has been obtained from the signal strength  $S$  and  $S_0$  in the presence and absence, respectively, of a diffusion-sensitive field gradient  $g$  (Stejskal and Tanner, 1965):

$$D = -\frac{1}{\gamma^2 g^2 (\Delta - \delta/3)} \ln \left( \frac{S}{S_0} \right),$$

where  $\gamma$  is the gyromagnetic ratio of  $^1\text{H}$ ,  $\delta$  is the duration of the gradient pulse and  $\Delta$  the observation time between pulses (the denominator is often referred to as the  $b$  value). Here, we have averaged measurements in the three principal directions, as the method employed did not allow for derivation of the full diffusivity tensor (cf. Menzel, 2002). In the absence of convective transport, self-diffusion in the free liquid is limited by the self-diffusivity of water  $D(\text{H}_2\text{O})$ . Here,  $D(\text{H}_2\text{O})$  has been derived based on Pruppacher's (1972) approach, with the dynamic viscosity of brine parameterized as a function of temperature and salinity (Cox and Weeks, 1975). While bulk diffusivities at temperatures of  $-15^{\circ}\text{C}$  or above come close to those of the free liquid (see ratio between diffusivity in ice and in free liquid; Fig. 4), we did not find any evidence of convective transport as described by Callaghan and others (1999). At the lowest measured temperatures, the apparent diffusivities are up to an order of magnitude smaller than those expected for free water.

This latter observation is interpreted to be a result of significant constriction of Brownian motion, characterized by a diffusion length scale of  $L = (2D\Delta)^{1/2}$ , within the pores at the observation time-scale  $\Delta = 19$  ms. As  $L$  approaches the characteristic pore dimension  $d$  with a decrease in pore size at lower temperatures (Fig. 2), the apparent diffusivity drops well below that of the free liquid. Plotting the apparent diffusivity as a function of the bulk liquid volume fraction demonstrates how the reduction in  $L$  for brine-volume fractions  $<30\%$  can be interpreted to correspond to a decrease in pore size below  $L$  (Fig. 4).

#### 4. DISCUSSION AND CONCLUSIONS

The MR imaging demonstrated the increase in pore size associated with an increase in temperature from approximately  $-15$  to  $-3^{\circ}\text{C}$ , which agrees with previous findings (Eicken and others, 2000), extending the observations to higher temperatures. Increases in pore linear dimensions and cross-sectional area scale with total brine-volume fraction and are hence highest in the temperature interval  $-6$  to  $-3^{\circ}\text{C}$ . This finding is commensurate with a thin-section warming experiment conducted by Perovich and Gow (1996) and results from an equivalent cross-sectional area model by Light and others (2003). The inclusion number density calculated from the probability density function of pore cross-sectional area for the present dataset exhibits similar characteristics to the measurements obtained by Perovich and Gow (1996) and Light and others (2003) for first-year Arctic sea ice from thin-section analysis (Fig. 5). With an increase in temperature, number densities shift towards larger cross-sectional areas. At the same time, for some samples, we observed an apparent increase in the number density. Thin-section analysis (Perovich and Gow, 1996) and an earlier MRI study (Eicken and others, 2000) have yielded comparable results. As the detailed examination of the individual section data indicates (Figs 1 and 3), this is not due to segregation of individual pores but simply a question of resolution, such that the number density of the population of pores too small to be detected by MRI at lower temperatures is shifted towards pore sizes large enough to be detected at higher temperatures. This problem of a size detection limit is particularly relevant for lognormal pore-size distributions (Fig. 5). It may also explain the low brine-volume fractions derived for the columnar ice sample with significantly smaller pore sizes than the corresponding granular ice sample, in particular at lower temperatures (Fig. 2). Examination of larger pores indicates that brine inclusions tend to merge into larger connected features upon warming (Fig. 3).

Transport properties such as permeability depend strongly on pore connectivity, and while pore-size variables scale with total brine-volume fraction we did not find any direct evidence of a disproportionate increase in the pore connectivity, as manifested, for example, in the number density or cross-sectional area of pores. Given the significant errors in estimating the bulk liquid porosity from MRI data (Fig. 2a) and as a note of caution, we conclude that at this stage the quantitative accuracy of the approach employed here does not allow for an in-depth examination of linkages between pore connectivity and permeability. In this context, one also needs to consider the potential impact of sample cooling after core extraction. While the magnitude of the cooling is comparable to that experienced by natural sea ice during the course of the winter, it still needs to be verified to what extent hysteretic pore connectivity and shape evolution can differ between a natural and a laboratory setting.

Nevertheless, for the larger pores sampled by the MRI sections, some linking and merging was apparent (Fig. 3), though not manifest in pore microstructural variables due to the resolution dependence of these variables discussed above. A further limitation in the method is the spacing of several millimeters between adjacent MRI slices. This was dictated by the constraints of reasonable image-acquisition time and the avoidance of sample heating, but precludes the identification of three-dimensionally connected pore space

networks. The latter is probably better served by X-ray microtomographic techniques that are not subject to such limitations. The examination of individual pore networks, in columnar and even more so in granular ice, revealed complex pore shapes that do not necessarily conform with Assur's (1960) merging cylinder model. Figure 3 demonstrates how (near)-isometric sub-millimeter pores (many of them too small to be resolved individually) join up into brine inclusions several millimeters across as the sample is warmed. It will require further work to determine what controls the morphology of pores such as those shown in Figure 3b, but the evidence presented here and in studies by Perovich and Gow (1996) and Light and others (2003) suggests that at the microscale the role of sub-resolution pores in controlling pore connectivity needs to be examined in more detail.

Derivation of the bulk sample  $^1\text{H}$  MR diffusivity is one means of probing the unresolved pore-size fraction. Despite limitations in the observation time length  $\Delta$ , we have observed a distinct temperature dependence of the characteristic diffusion length, that allows conclusions about constriction of pores to sizes  $<3\ \mu\text{m}$  at  $-15^\circ\text{C}$ , and  $<1\ \mu\text{m}$  at temperatures around  $-28^\circ\text{C}$ . Such small pore sizes at low temperatures correspond well with direct microscopic measurements that revealed characteristic pore sizes ranging between about 1 and  $5\ \mu\text{m}$  at  $-15^\circ\text{C}$  and below (A. Stierle and others, unpublished data) and are also commensurate with observations of a network of liquid veins and nodes in fresh-water ice (Mader, 1992). At the same time, we can expect hydrohalite precipitation to have a significant influence on mean free-path lengths at temperatures below about  $-25^\circ\text{C}$  as the remaining brine inclusions fill with a dense mixture of salt precipitates, brine and potentially ice (Bock and others, 2003; Light and others, 2003; A. Stierle and others, unpublished data). We did not find any evidence for enhanced diffusivity suggestive of convective transport as observed by Callaghan and others (1999). In part, this may be due to the absence of artificially imposed large-scale hydraulic gradients such as present in the experimental set-up of Callaghan and co-workers.

Pore microstructure differs substantially between granular and columnar ice over the entire temperature range (Figs 2 and 5). These differences are in large part explained by the obvious ties between pore and grain microstructure (Fig. 1) and the contrasts in the initial brine entrapment process for frazil as opposed to congelation ice. Furthermore, the MR diffusivity measurements (Fig. 4) indicate that even in the low-temperature regime substantial differences exist between the two ice types. While one could hypothesize that these contrasts are driven by interfacial processes and the crystallography of pore boundaries, with granular ice largely containing intergranular inclusions (Fig. 1d and e) as opposed to mostly intragranular inclusions in columnar ice (Fig. 1a and b), further work is needed to enhance the sensitivity and quantitative accuracy of the method as employed here.

## ACKNOWLEDGEMENTS

This work has been supported by US National Science Foundation, Office of Polar Programs grants OPP-9817738 and 0222312. We thank R. Wittig and P. Cotter for help in the laboratory, and H.-O. Poertner for support and providing MRI laboratory access. Field sampling was well supported

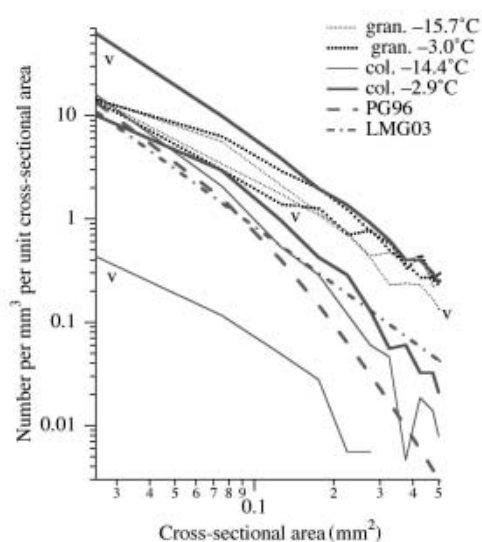


**Fig. 5.** Brine inclusion number density (expressed as a probability density, i.e. normalized to unit cross-sectional area for a bin width of  $0.05\ \text{mm}^2$ ) as a function of inclusion cross-sectional area for low and high temperatures. Data obtained from vertical sections are marked by a 'v'; all other curves are derived from horizontal sections. Also shown are number density distributions obtained by Perovich and Gow (1996) (PG96) and Light and others (2003) (LMG03, extrapolated beyond LMG03's maximum pore size of  $0.03\ \text{mm}^2$ ).

by the Barrow Arctic Science Consortium. Constructive comments by two anonymous reviewers helped to improve the manuscript.

## REFERENCES

- Assur, A. 1960. Composition of sea ice and its tensile strength. *CRREL Res. Rep.* 44.
- Bock, C., H. Eicken, and R.M. Wittig. 2005.  $^{23}\text{Na}$  NMR spectroscopy and diffusion weighted MRI studies on sea-ice at different temperature: the influence of environmental effects on ice growth. *Proceedings of the 11th Annual Meeting of the International Society for Magnetic Resonance in Medicine, Toronto, Canada, 10–16 July, 2003*, 883. St Louis, MO: Mira Digital Publishing.
- Callaghan, P.T., R. Dykstra, C.D. Eccles, T.G. Haskell and J.D. Seymour. 1999. A nuclear magnetic resonance study of Antarctic sea ice brine diffusivity. *Cold Reg. Sci. Technol.*, **29**(2), 153–171.
- Cox, G.F.N. and W.F. Weeks. 1975. Brine drainage and initial salt entrapment in sodium chloride ice. *CRREL Res. Rep.* 345.
- Cox, G.F.N. and W.F. Weeks. 1983. Equations for determining the gas and brine volumes in sea-ice samples. *J. Glaciol.*, **29**(102), 306–316.
- Edelstein, W.A. and E.M. Schulson. 1991. NMR imaging of salt-water ice. *J. Glaciol.*, **37**(125), 177–180.
- Eicken, H., C. Bock, R. Wittig, H. Miller and H.O. Poertner. 2000. Nuclear magnetic resonance imaging of sea-ice pore fluids: methods and thermal evolution of pore microstructure. *Cold Reg. Sci. Technol.*, **31**(3), 207–225.
- Eicken, H., H.R. Krouse, D. Kadko and D.K. Perovich. 2002. Tracer studies of pathways and rates of meltwater transport through Arctic summer sea ice. *J. Geophys. Res.*, **107**(C10), 8046. (10.1029/2000JC000583.)
- Freitag, J. 1999. Untersuchungen zur Hydrologie des arktischen Meereises – Konsequenzen für den kleinskaligen Stofftransport. *Ber. Polarforsch/Rep. Pol. Res.* 325.

- Golden, K.M., S.F. Ackley and V.I. Lytle. 1998. The percolation phase transition in sea ice. *Science*, **282**(5397), 2238–2241.
- Hudier, E.J.J., R.G. Ingram and K. Shirasawa. 1995. Upward flushing of sea water through first year sea ice. *Atmosphere–Ocean*, **33**(3), 569–580.
- Kawamura, T. 1988. Observations of the internal structure of sea ice by X-ray-computed tomography. *J. Geophys. Res.*, **93**(C3), 2342–2350.
- Krembs, C., R. Gradinger and M. Spindler. 2000. Implication of brine channel geometry and surface area for the interactions of sympagic organism in Arctic sea ice. *J. Exp. Mar. Biol. Ecol.*, **243**(1), 55–80.
- Light, B., G.A. Maykut and T.C. Grenfell. 2003. Effects of temperature on the microstructure of first-year Arctic sea ice. *J. Geophys. Res.*, **108**(C2), 3051. (10.1029/2001JC000887.)
- Lytle, V.I. and S.F. Ackley. 1996. Heat flux through sea ice in the western Weddell Sea: convective and conductive transfer processes. *J. Geophys. Res.*, **101**(C4), 8853–8868.
- Mader, H.M. 1992. Observations of the water-vein system in polycrystalline ice. *J. Glaciol.*, **38**(130), 333–347.
- Menzel, M.I. 2002. *Multi-nuclear NMR on contaminated sea ice*. Aachen, Shaker Verlag.
- Menzel, M., S. Han, S. Stapf and B. Blumich. 2000. NMR characterization of the pore structure and anisotropic self-diffusion in salt water. *J. Magn. Reson.*, **143**(2), 376–381.
- Perovich, D.K. and A.J. Gow. 1996. A quantitative description of sea ice inclusions. *J. Geophys. Res.*, **101**(C8), 18,327–18,343.
- Pruppacher, H.R. 1972. Self-diffusion coefficient of supercooled water. *J. Chem. Phys.*, **56**(1), 101–107.
- Stejskal, E.O. and J.E. Tanner. 1965. Spin diffusion measurements: spin echos in the presence of a time dependent field gradient. *J. Chem. Phys.*, **42**(1), 288–292.
- Weeks, W.F. 2001. NARL and research on sea ice and lake ice. In Norton, D.W., ed. *Fifty more years below zero*. Fairbanks, AK, University of Alaska Press, 177–186.
- Wettlaufer, J.S., M.G. Worster and H.E. Huppert. 2000. Solidification of leads: theory, experiment, and field observations. *J. Geophys. Res.*, **105**(C1), 1123–1134.